Structural and Reactive Evolution of Oxidatively Grafted Pd Catalysts on MnO2 for the Low-Temperature Oxidation of CO

SCHOLARONE™
Manuscripts

COMMUNICATION

Structural and Reactive Evolution of Oxidatively Grafted Pd Catalysts on MnO₂ for the Low-Temperature Oxidation of CO

Jacklyn N. Hall,[a] A. Jeremy Kropf,*[a] Uddhav Kanbur,[a] Fulya Dogan,[a] Carly Byron,[a] Jianguo Wen,[b] Massimiliano Delferro,*[a] and David M. Kaphan*[a]

Isolated Pd atoms supported on high surface area MnO₂, prepared by the oxidative grafting of (bis(tricyclohexylphosphine-palladium(0)), catalyze (> 50 turnovers, 17 h) the low temperature (≤ 325 K) oxidation of CO (7.7 kPa O₂, 2.6 kPa CO) with results of *in-situ/operando* and *ex situ* spectroscopic characterization signifying a synergistic role of Pd and MnO₂ in facilitating redox turnovers.

Precious metal catalysts, such as Au, Pt, and Pd, have been demonstrated to facilitate a wide range of industrially-relevant reactions including the oxidation of CO to CO_2, for which their activity and stability has been extensively evaluated.[1–5] Cooperativity between supported metal ions or nanoparticles with oxide supports of superior oxygen affinity has been considered crucial for low temperature (< 423 K)[6] CO oxidation due to synergistic action of the metal and surface.[2,7–10] In the case of Pd, it has been proposed that reducible oxides including FeO_x,[11] CeO_2,[4,12] and MnO_x,[13,14] aid in facilitating the reaction by providing labile oxygen at Pd-MO_x interfaces and play a central role in stabilizing isolated atoms that dictate the catalyst performance and efficiency.[2,15] Previous evaluations have also indicated that the speciation of Pd delineates activity at low temperatures (< 423 K) where metallic Pd is significantly less active than ionic Pd^{2+} or PdO_x clusters due to inhibition from the strong affinity of Pd(0) toward CO.[4,5,9,11,16] However, the interconversion of site-isolated Pd to nanoparticles under reducing reaction conditions often underlines catalyst deactivation.[9,17,18] For instance, even at room temperature, CO induces Pd sintering on Fe_2O_3(001) despite relatively low surface coverages of Pd (0.2 monolayers).[19] Further, there is an incentive to evaluate supported Pd catalysts that benefit from high reactivity but are resistant to sintering under reducing conditions for low temperature CO oxidation applications.

Recently, our group has demonstrated the well-defined interstitial doping of Ni on $Li_xMn_2O_4$ by an electron transfer mechanism between the oxidizing surface and the low-valent precursor (Ni(COD)₂, COD = cyclooctadiene).[20] We reason this strategy may afford well anchored isolated sites for comparable group 10 systems, particularly for resistance to agglomeration under reducing conditions. Herein, this oxidative grafting technique is applied to introduce Pd onto MnO₂ as a targeted oxidation catalyst. Specifically, the well-defined precursor Pd(PCy₃)₂ (PCy₃ = tricyclohexylphosphine) was added to a suspension of MnO₂ in benzene at room temperature for 48 hours to produce **Pd/MnO₂** with approximately 1.1 wt% Pd (details in Section S1.1, SI). The resulting material is found to be an efficient catalyst for the low-temperature oxidation of CO with O₂ between room temperature (295 K) and 323 K which is comparable to temperature ranges (303 - 398 K) for the activity of other recently developed catalysts for this chemistry.[2,3,8,9] Atomically dispersed Pd active sites are evidenced on the oxide surface, of which a majority (roughly 80%) remain isolated during reaction (2.6 kPa CO, 7.7 kPa O₂) at 323 K over 7 hours. Further, a combination of *in situ/operando* and *ex situ* characterization results indicate a dual-role of Pd and the MnO₂ surface in enabling the catalytic activity.

High-surface area MnO₂ (277 m² g⁻¹) was utilized as a catalyst support to promote sufficient grafting of Pd(PCy₃)₂. The material consists of amorphous and needle-like particles (Figure S2), with perceptible synchrotron X-ray diffraction peaks coinciding with a Birnessite structure (Figure S1). Upon grafting of the zero-valent Pd(PCy₃)₂ precursor (Figure 1a), there is an
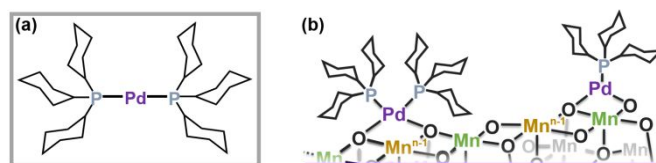
[a.] Chemical Sciences and Engineering Division, Argonne National Laboratory, Lemont, Illinois 60439, USA. Email: kaphand@anl.gov, delferro@anl.gov, kropf@anl.gov

[b.] Center for Nanoscale Materials, Argonne National Laboratory, Lemont, Illinois 60439, USA. Email: jwen.anl.gov

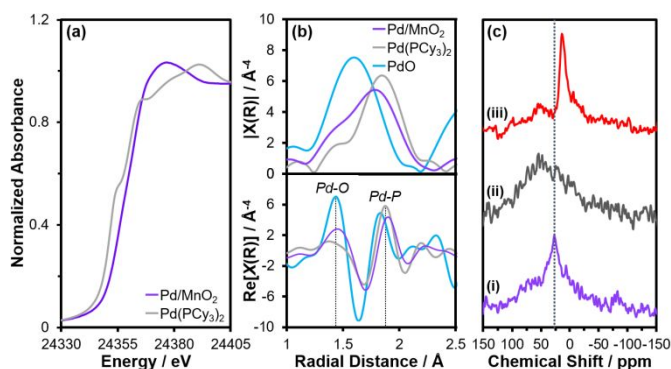**Figure 1.** Schematic of (a) Pd(PCy₃)₂ and (b) the potential structures of Pd/MnO₂.

Figure 2. Pd K-edge (a) XANES and (b) χ(R) spectra for fresh Pd/MnO₂ in comparison to PdO and the Pd(PCy₃)₂ precursor (k^3-weighted k = 3 – 13.8 Å⁻¹, Δk = 0.1). (c) ³¹P solid-state NMR for (i) fresh Pd/MnO₂, (ii) post-catalysis (7 h, 323 K, 2.6 kPa CO, 7.7 kPa O₂) and (iii) post O₂ regeneration (573 K, 10% O₂, 1.5 hours, 1 cycle).

Figure 4. (a) *Ex situ* Pd K-edge EXAFS for Pd/MnO₂ reduced (150 °C 5% CO, 1.5 h) and post-catalysis (323 K, 7.71 kPa O₂, 2.56 kPa CO, 7 hours) (k = 3.0 – 11.1 Å⁻¹, Δk = 0.1, k^3-weighted). (b) Pd K-edge XANES LCF result for the post-catalysis Pd/MnO₂ sample using the Pd foil and fresh Pd/MnO₂ as standards.

apparent electron transfer from the metal complex to the oxide surface as indicated by an increase in Pd oxidation state and a slight reduction in the bulk Mn oxidation state as reflected in the Pd and Mn K-edge X-ray absorption near edge structures (XANES), (Figure 2a and Figure S3). Qualitative comparison of the Pd extended X-ray absorption fine structure (EXAFS) with PdO and Pd(PCy₃)₂ (Figure 2b) suggests that Pd/MnO₂ features both Pd-O and Pd-P bonds in the first coordination shell that account for the shorter and longer radial components, respectively. EXAFS fitting results indicate the Pd species may form a combination of 3 or 4 coordinate complexes with 1-2 oxygen and 1-2 phosphine ligands (Table S1, Figure 1b), suggesting that the Pd ions retain their molecular speciation upon chemisorption as isolated species on the surface of MnO₂. Evaluation of the phosphorous chemical environment by ³¹P solid-state NMR further evidences the persistence of metal-bound phosphine ligands at δ = 26.4 ppm (Figure 2c), consistent with the chemical shift to cationic Pd-bound PCy₃ (δ = 25.4 ppm, Pd(PCy₃)₂Cl₂)[21] and 39.7 ppm of the precursor (Pd(PCy₃)₂).[22]

To investigate the catalytic properties of Pd/MnO₂ for CO oxidation, the reactivity was explored between room temperature (295 K) and 323 K. Introduction of CO to the catalyst under O₂ flow at 295 K results in a finite burst of CO₂ formation that tapers to rates below the detection limit after approximately 400 minutes and roughly 11 mol CO₂ (mol Pd)⁻¹ formed (Figure 3a), demonstrating the highly oxidizing nature of the catalyst, unlike the parent MnO₂ which does not form
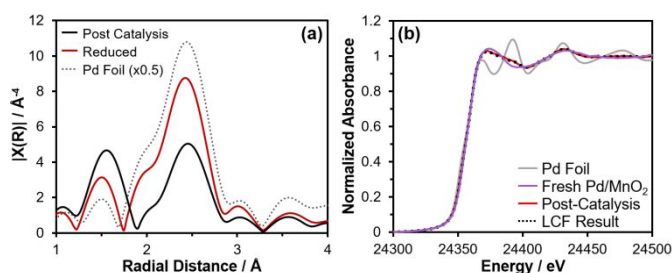
measurable quantities of CO₂ under the conditions tested. Slightly elevated reaction temperatures (323 K) result also in a short-term, highly reactive state of the catalyst (Figure 3b); however, this is followed by CO₂ formation rates that decay to lower, relatively stable rates after 2 – 3 hours of reaction (Figure S15). For fresh Pd/MnO₂ this results in over 50 mol CO₂ per mol Pd during 1060 minutes of reaction at 323 K (Figure 3c).

Due to the prevalence of CO-induced Pd sintering in supported catalysts,[9,19] the influence of Pd agglomeration toward the observed catalyst deactivation was investigated. *Ex situ* EXAFS characterization of Pd/MnO₂ post 7 hours of reaction at 323 K indicates the formation of Pd nanoparticles by the presence of the Pd-Pd scattering feature at a phase uncorrected distance of roughly 2.45 Å (Figure 4a). Linear combination fitting (LCF) of the XANES and EXAFS of the post-catalysis sample with (i) the as-prepared material and (ii) Pd metal indicates approximately only 20% is reduced to a metallic state (Table S2, Figure 4b, S6-S7), while 80% remains isolated. EXAFS fitting results (Table S3) indicate that the agglomerated Pd forms large nanoparticles as a minor species, as the average Pd-Pd bond length (2.737 ± 0.007 Å) in the post-catalysis sample is close to bulk Pd (2.740 ± 0.004 Å), further supporting the use of the Pd foil as a reasonable standard for the LCF. Correspondingly, TEM images show the formation of large (10.8 ± 4.8 nm) Pd nanoparticles (Figure S2). To better understand the role of metallic Pd, further reduction was induced by treatment of Pd/MnO₂ with 10% CO at 423 K. The XANES of reduced Pd/MnO₂ indicates a close correspondence with Pd metal (Figure S9) with the EXAFS showing a significant increase in the fraction of Pd nanoparticles in comparison to the post-catalysis
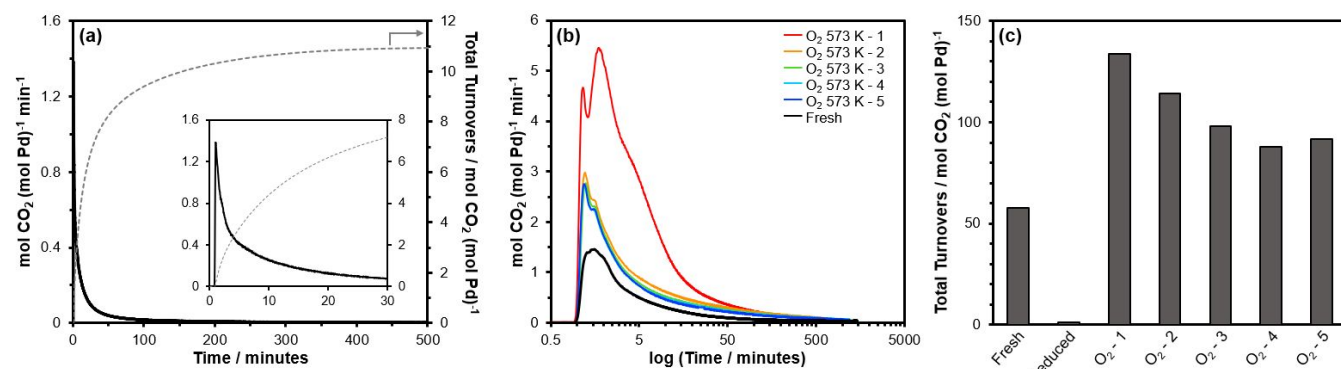

Figure 3. (a) CO oxidation at 295 K for fresh Pd/MnO₂, (b) CO oxidation at 323 K for fresh Pd/MnO₂ or following O₂ regeneration (573 K, 1.5 h, 10% O₂/He) for 1 – 5 cycles, and (c) turnover numbers (mol CO₂ (mol Pd)⁻¹) over 1060 minutes (or until CO₂ formation ceased) for Pd/MnO₂ fresh, reduced, or following O₂ regeneration for 1 – 5 cycles. (Reaction conditions: 7.71 kPa O₂, 2.56 kPa CO, 50 mL min⁻¹, 20 mg catalyst). "O₂ (573 K) - #" refers to the number (#) of O₂ regeneration cycles.

COMMUNICATION

sample by the higher amplitude of the Pd-Pd scattering feature at 2.45 Å (Figure 4a). The catalyst pre-reduced at 423 K in CO shows only trace CO_2 formation under the standard reaction conditions at 323 K (Figure S16) resulting in only 1.1 mol CO_2 formed per mol Pd (Figure 3c). This observation underscores the role of isolated Pd in the catalytic redox performance at low temperature and that, even at extended reaction times, the diminished but non-zero CO_2 formation rates measured are unlikely to originate from metallic Pd domains (Figure S15).

Operando XAFS measurements of Pd and Mn in the catalyst were conducted to investigate the transient structure evolutions that delimit the CO oxidation reactivity between room temperature and 323 K. First, monitoring of the Pd K-edge during reaction at room temperature indicates a gradual change in the first-shell coordination environment by an apparent shift in the EXAFS peak to lower radial distance (Figure 5a). This change is further enhanced upon ramping temperature to 323 K at 0.24 K min^{-1} (Figure 5a) and appears related to fewer phosphine ligands that comprise the higher radial-component of the first-shell in the X(R) spectra (Figure 5b), consistent with *ex situ* NMR measurements completed after 7 hours of reaction indicating a downward shift in the ^{31}P resonance compared to the fresh Pd/MnO$_2$ (Figure 2c). Near 323 K, the onset of Pd sintering is apparent from the scattering peak at 2.45 Å in Figure 5c which continues to grow in intensity while holding at 323 K over the course of 2 hours. Fitting of the EXAFS spectra (Table S5, SI) indicates the average Pd-Pd coordination number (CN) increases linearly with time at 323 K (Figure 5d), although monitoring of the gas effluent provides that the decaying of CO_2 formation rates begins to slow after 2h (Figure 5d), which is consistent with off-line reaction experiments (Figure S14). Moreover, by comparison with the *ex situ* post-catalysis sample measured after 7 hours of reaction (Figure S19), it is apparent that nanoparticle formation continues relatively monotonically with time on stream and lacks sufficient correlation with the short-term catalyst deactivation to be directly responsible.

Mn K-edge XAFS measurements indicate an influence of the reaction conditions on the properties of the support.
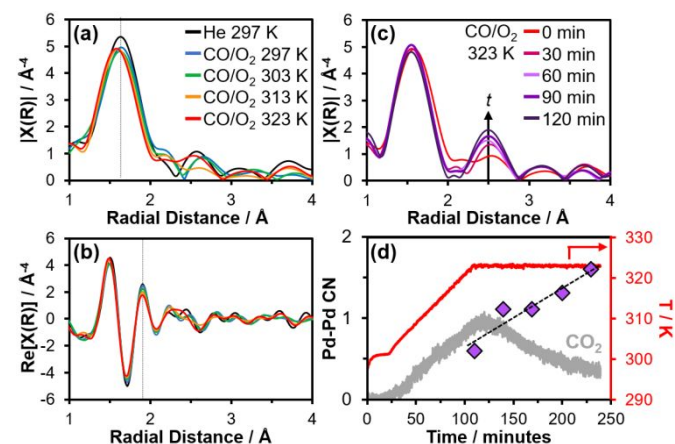

Figure 5. XAFS analysis of Pd/MnO$_2$ during operando CO oxidation, measuring the Pd K-edge showing (a) changes in ⌈X(R)⌉ and (b) the real component of X(R) upon exposure to CO and O$_2$ at room temperature (297 K) and during temperature ramping to 323 K; (c) changes in |X(R)| under reaction conditions at 323 K; (d) CO$_2$ signal (gray) and (◆) Pd-Pd coordination number (CN) fit from the EXAFS data as a function of time and temperature (red) during reaction.
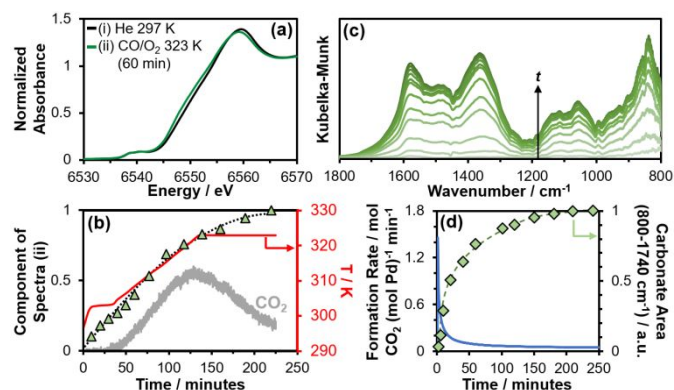

Figure 6. XAFS of Pd/MnO$_2$ during operando CO oxidation, measuring the Mn K edge, showing (a) changes in the absorption edge between the fresh material and at the end of the experiment; and, (b) as a function of time and temperature, the CO$_2$ signal (gray) and the corresponding shift in the Mn absorption edge (▲) to lower energy estimated by a linear combination of spectra (i) and (ii) from Figure 6a where the y-axis value is the component of spectra (ii). (c) *In situ* DRIFTS of fresh Pd/MnO$_2$ during CO oxidation at 323 K and (d) the corresponding CO$_2$ formation rate and area of the infrared spectra from 800-1740 cm^{-1} with time under reaction conditions.

Specifically, there is a gradual shift in the absorption edge to lower energy upon exposure to CO and O$_2$ at 297 K and during ramping and holding at 323 K for 1 hour (Figure S20) that evidences a decrease in the average Mn oxidation state. A LCF for each sample measured between the start and end of the experiment (Figure 6a) indicates there is a non-linear shift in the Mn edge to lower energy (Figure 6b), particularly during ramping to 323 K, which suggests a deceleration in the rate of Mn reduction at this point. To accompany analysis of surface changes during reaction, *in situ* DRIFTS (diffuse reflectance infrared Fourier transform spectroscopy) measurements were completed. Upon exposure to CO under O$_2$ flow at 323 K, Pd/MnO$_2$ displays rapid growth of several intense bands in the region from 800 – 1740 cm^{-1} that decelerate to near saturation after about 90 minutes (Figure 6c,d). The species observed are in close correspondence with mono- and multidentate carbonate bands previously identified on Mn$_2$O$_3$ and Ni$_x$Mn$_{3-x}$O$_4$ upon reaction with CO.[13,23] In conjunction with XAFS results indicating the progressive reduction of Mn (Figure 6a,b), it is evident that the evolution and growth of carbonates occluding the MnO$_2$ surface, in combination with the potential formation of oxygen vacancies, may have a significant influence on initial deactivation (< 2 h) of the catalyst, unlike Pd agglomeration which occurs slowly and linearly at this timescale (Figure 5d).

The regenerability of Pd/MnO$_2$ following CO oxidation at 323 K was assessed by completing cycles of O$_2$ treatment at 573 K following reaction at 323 K. Results indicate that the catalytic reactivity can be restored above that of the fresh catalyst through the 573 K treatment (Figure 3b). Specifically, 1 cycle of reaction and O$_2$ treatment (O$_2$ -1) results in 2.3x increase in the number of turnovers from 57 to 139 mol CO$_2$ (mol Pd)$^{-1}$ over 1060 minutes at 323 K (Figure 3c). A minor decline in the cumulative CO$_2$ formed is observed between the second (O$_2$-2) and third (O$_2$-3) cycles of reaction and regeneration (Figure 3c), although CO$_2$ formation rates measured at extended reaction times (approximately > 600 minutes) approach comparable values (Figure S15) for the total of 5 cycles evaluated. *In situ* DRIFTS measurements of Pd/MnO$_2$ treated to 573 K under 10% O$_2$ reveals degradation of the PCy$_3$ ligands by the disappearance of their characteristic absorption bands in the spectra (Figure

S22b) with solid-state ^{31}P NMR measurements being suggestive of phosphate formation based on the chemical shift (12.9 ppm) of the oxidized species (Figure 2c). Additional *in situ* DRIFTS measurements of fresh and regenerated Pd/MnO_2 during CO oxidation at 323 K indicate that surface carbonates formed during reaction are diminished following O_2 treatment at 573 K (Figure S22a) and that carbonate coverages during reaction increase substantially after regeneration (Figure S23). Further, regeneration of the surface by carbonate removal as well as the accessibility of additional surface sites (following liberation of the bulky cyclohexane ligands) may both contribute to the initial higher reactivity of the O_2 regenerated catalyst.

Characterization of the Pd speciation following 1 cycle of O_2 regeneration and catalysis indicates that the Pd is partially re-oxidized by the shift in the Pd absorption edge to higher energy (Figure S10b) and a corresponding increase in the intensity of the Pd-O scattering in the EXAFS (Figure S10a). Persistence of a metallic Pd phase is apparent from the peak at a phase uncorrected distance of roughly 2.47 Å in the EXAFS (Figure S10a) and suggests an oxide layer may form on the surface of the metal particles, consistent with observations of Nolte *et al* for large Pd particles (> 9 nm) on MgO that form a thin PdO surface layer under comparable conditions (570 K, $0.03 - 0.056$ kPa O_2).[24] Moreover, O_2 regeneration is insufficient to produce measurable CO_2 formation rates past roughly 100 minutes of reaction for both reduced Pd/MnO_2 (featuring predominantly Pd nanoparticles, Figure 4a) and bare MnO_2 (Figure S18, Table S4) indicating the vital role of isolated Pd in Pd/MnO_2 both after reaction and regeneration, although re-oxidation of the oxide surface may contribute to the finite quantities of CO_2 formed over MnO_2 and reduced Pd/MnO_2 (Table S4).

In conclusion, Pd/MnO_2 synthesized by the oxidative grafting of $Pd(PCy_3)_2$ forms isolated Pd active sites for CO oxidation, of which, only roughly 20% undergo agglomeration to Pd nanoparticles, a common pitfall of precious metal catalysts for low-temperature CO oxidation, during reaction at 323 K for 7 hours. A combination of time-resolved characterization results reveal the structural changes which occur to Pd and MnO_2 during reaction and suggest that reduction and blocking of MnO_2 by carbonate formation may contribute to short-term deactivation; however, the initial catalyst reactivity can be restored above that of the fresh material through regeneration at 573 K in 10% O_2. Cooperative action of the isolated Pd and oxide surface is essential toward the low temperature redox activity; this and the role of each species in the catalytic cycle will be the subject of future studies.

Conflicts of interest

There are no conflicts to declare.

Notes and references

1   M. Haruta, N. Yamada, T. Kobayashi and S. Iijima, *J Catal*, 1989, **115**, 301–309.
2   K. Yuan, Y. Guo, L. Huang, L. Zhou, H. J. Yin, H. Liu, C. H. Yan and Y. W. Zhang, *Inorg Chem*, 2021, **60**, 4207–4217.
3   L. Nie, D. Mei, H. Xiong, B. Peng, Z. Ren, X. I. P. Hernandez, A. DeLaRiva, M. Wang, M. H. Engelhard, L. Kovarik, A. K. Datye and Y. Wang, *Science (1979)*, 2017, **358**, 1419–1423.
4   T. Bunluesin, E. S. Putna and R. J. Gorte, *Catal Letters*, 1996, **41**, 1–5.
5   P. J. Berlowitz, C. H. F. Peden and D. W. Goodman, *Journal of physical chemistry*, 1988, **92**, 5213–5221.
6   USDRIVE Advanced Combustion and Emission Control Roadmap.
7   R. Xu, X. Wang, D. Wang, K. Zhou and Y. Li, *J Catal*, 2006, **237**, 426–430.
8   R. K. Kunkalekar and A. v. Salker, *Reaction Kinetics, Mechanisms and Catalysis*, 2013, **108**, 173–182.
9   E. J. Peterson, A. T. DeLaRiva, S. Lin, R. S. Johnson, H. Guo, J. T. Miller, J. H. Kwak, C. H. F. Peden, B. Kiefer, L. F. Allard, F. H. Ribeiro and A. K. Datye, *Nature Communications 2014 5:1*, 2014, **5**, 1–11.
10 S. Imamura, H. Sawada, K. Uemura and S. Ishida, *J Catal*, 1988, **109**, 198–205.
11 L. Wang, C. Pu, L. Xu, Y. Cai, Y. Guo, Y. Guo and G. Lu, *Fuel Processing Technology*, 2017, **160**, 152–157.
12 M. F. Luo, Z. Y. Hou, X. X. Yuan and X. M. Zheng, *Catal Letters*, 1998, **50**, 205–209.
13 S. Imamura, Y. Tsuji, Y. Miyake and T. Ito, *J Catal*, 1995, **151**, 279–284.
14 J. S. Park, D. S. Doh and K. Y. Lee, *Top Catal*, 2000, **10**, 127–131.
15 A. I. Boronin, E. M. Slavinskaya, I. G. Danilova, R. v. Gulyaev, Y. I. Amosov, P. A. Kuznetsov, I. A. Polukhina, S. v. Koscheev, V. I. Zaikovskii and A. S. Noskov, *Catal Today*, 2009, **144**, 201–211.
16 Y. F. Y. Yao, *J Catal*, 1984, **87**, 152–162.
17 T. M. Lardinois, K. Mandal, V. Yadav, A. Wijerathne, B. K. Bolton, H. Lippie, C. W. Li, C. Paolucci and R. Gounder, *Journal of Physical Chemistry C*, 2022, **126**, 8337–8353.
18 S. Hinokuma, H. Fujii, M. Okamoto, K. Ikeue and M. Machida, *Chemistry of Materials*, 2010, **22**, 6183–6190.
19 G. S. Parkinson, Z. Novotny, G. Argentero, M. Schmid, J. Pavelec, R. Kosak, P. Blaha and U. Diebold, *Nature Materials 2013 12:8*, 2013, **12**, 724–728.
20 A. Chapovetsky, R. M. Kennedy, R. Witzke, E. C. Wegener, F. Dogan, P. Patel, M. Ferrandon, J. Niklas, O. G. Poluektov, N. Rui, S. D. Senanayake, J. A. Rodriguez, N. J. Zaluzec, L. Yu, J. Wen, C. Johnson, C. J. Jenks, A. J. Kropf, C. Liu, M. Delferro and D. M. Kaphan, *ACS Catal*, 2022, **12**, 7233–7242.
21 V. v. Grushin, C. Bensimon and H. Alper, *Inorg Chem*, 1994, **33**, 4804–4806.
22 M. Tanabe, N. Ishikawa and K. Osakada, *Organometallics*, 2006, **25**, 796–798.
23 C. Laberty, C. Marquez-Alvarez, C. Drouet, P. Alphonse and C. Mirodatos, *J Catal*, 2001, **198**, 266–276.
24 P. Nolte, A. Stierle, N. Kasper, N. Y. Jin-Phillipp, H. Reichert, A. Rühm, J. Okasinski, H. Dosch and S. Schöder, *Phys Rev B*, 2008, **77**, 115444.